Supplementary Information for

Topological Spin/structure Couplings in Layered Chiral Magnet Cr$_{1/3}$TaS$_2$- the Discovery of Spiral Magnetic Superstructure

Kai Du[a], Fei-Ting Huang[a], Jaewook Kim[a], Seong Joon Lim[a], Kasun Gamage[b], Junjie Yang[b,c], Maxim Mostovoy[d], Joseph Garlow[e], Myung-Geun Han[e], Yimei Zhu[e], and Sang-Wook Cheong[a]*

[a] Rutgers Center for Emergent Materials and Department of Physics and Astronomy, Rutgers University, Piscataway, New Jersey 08854, USA

[b] Department of Physics, Central Michigan University, Mount Pleasant, MI 48858, USA

[c] Department of Physics, New Jersey Institute of Technology, Newark, New Jersey 07102, USA.

[d] Zernile Institute for Advanced Materials, University of Groningen, Nijenborgh 4, 9747 AG Groningen, Netherlands

[e] Condensed Matter Physics and Materials Science Department, Brookhaven National Laboratory, Upton, New York 11973, USA

* Corresponding to Sang-Wook Cheong.

Email: sangc@physics.rutgers.edu

This PDF file includes:

Supplementary text Note 1- Note 3
Figures S1 to S10
SI References (SI ref. 1-4)

Supplementary Information Text

Note 1: Comparing helical spins in $Cr_{1/3}TaS_2$ and $Cr_{1/3}NbS_2$

According to (*8, 18*), the magnetic helical pitch length L can be defined as $L = 2\pi c* J_z/D_z$, where c is the lattice constant along the helical axis, J_z is the interlayer symmetric ferromagnetic exchange interaction, and D_z is the interlayer Dzyaloshinsky-Moriya (DM) interaction induced by the noncentrosymmetric crystal structure. Considering $Cr_{1/3}TaS_2$ and $Cr_{1/3}NbS_2$ have similar magnitudes of the *c*-lattice constant and J_z (same Cr^{3+} ions in a similar lattice), the helical pitch length L will only depend on D_z. The Dzyaloshinsky-Moriya (DM) interaction is determined by the combination of the structural chiral strength and the spin-orbit coupling. As the 5d element (Ta) in $Cr_{1/3}TaS_2$ can provide much stronger spin-orbit coupling than the 4d element (Nb) in $Cr_{1/3}NbS_2$, the smaller helical pitch of $Cr_{1/3}TaS_2$ ($L\approx15$ nm) can be expected as the consequence of a larger overall D_z value in $Cr_{1/3}TaS_2$.

Note 2: MFM working mechanism on helimagnets

The origin of MFM contrasts can be interpreted properly by considering the principle of MFM and magnetic properties of $Cr_{1/3}TaS_2$ together. The magnetic force (F) and the tip-sample distance (r) will follow the inverse square law if assuming monopole–monopole interaction between the tip and the sample: $F \propto 1/r^2$. For typical tapping-mode MFM, the directly-detected MFM response (phase change) is proportional to the magnetic force gradient (SI ref. 1) $dF/dr \propto 1/r^3$ (Fig. S7B). Therefore, MFM is relatively a surface-sensitive technique. In general, magnetic moments of typical atomic-scale antiferromagnetic or non-collinear spin structures will cancel with each other and give no MFM contrasts. However, the situation changes in helical spin structures with a long helical pitch. In this case, the surface sensitivity of MFM would still enable us to pick up magnetic signals as we show in our work. In $Cr_{1/3}TaS_2$, the MFM signals are dominated by those few layers close to the surface (Fig. S7A). Then, $Cr_{1/3}TaS_2$ can be effectively considered as a simple "in-plane ferromagnetic" material for MFM measurements (Fig. S7C) due to its long helical pitch ($L\approx15$ nm). Thus, different effective magnetic moments will show up if magnetic helical domains with different helicities are terminated at the surface, leading to a magnetic helical domain wall contrast. This is consistent with our MFM simulation in Fig. S7D. Depending on which layer is chosen, the angles between spins in two adjacent magnetic helical domains can be arbitrary. Although Fig. S7A only represents one possible situation, the same mechanism and results can be easily validated for all other possible spin configurations as long as they have different effective magnetic moments. Statistically, the possibility of having the same paralleled effective magnetic moments is extremely low due to the arbitrariness of spin directions in the *ab* plane. Therefore, almost all the magnetic helical domain walls are visible in MFM in reality.

For the simple helical spin order, spins within a single layer typically align parallelly due to ferromagnetic exchange interactions in the *ab* plane. However, spins within each magnetic helical domain may also rotate "in the *ab* plane" and form domains in a large length-scale to further minimize the magnetostatic energy. These additional magnetic

domains within magnetic helical domains are what we call magnetic antiphase domains. The same MFM contrast mechanism explained above is also valid for these broad magnetic antiphase domain contrasts where the only difference is the helicity is the same for magnetic antiphase domains along the *c* axis.

Note 3: Interlocked structural chirality and magnetic helicity

To further address the interplay between structural chiral domains (SCDs) and magnetic helical domains (MHDs) in $Cr_{1/3}TaS_2$, a part of the MFM image (Fig. 1G) is cropped in Fig. S8A for MFM simulations by using micromagnetic simulation software suite (Mumax3) (SI ref. 2). Without losing the generality, gradual magnetic antiphase domain contrasts are ignored to simplify the simulation. A possible effective magnetic moment configuration is proposed in Fig. S8B. The simulated MFM image in Fig. S8C resembles closely our experimental data while the characteristic antisymmetric line profiles are also clearly reproduced in Fig. S8D. Even though Fig. S8B is not the only possible configuration that could generate such MFM contrasts, we can still conclude that MFM can sense the stray field of those helical spin orders at the domain walls with a long-enough helical pitch and MHD walls are strongly coupled to SCD walls in $Cr_{1/3}TaS_2$. Note that this interlocking of the structural chirality and the magnetic helicity has been also observed in homochiral materials such as iron langasite (SI ref. 3) and some B20 compounds (SI ref. 4).

To prove the statement above, we have examined domain structures of the same area in different magnetic thermal cycles (referring to a heating up to 300 K and a cooling back to 80 K) (Fig. S9A and S9B). As interlocked by SCD walls, positions of sharp MHD walls are found to remain intact while magnetic antiphase domain patterns and their contrasts are dissimilar in different magnetic thermal cycles. Moreover, magnetic signals have no correlations with the topography as well as the EFM image, which disappear above the magnetic ordering temperature (Fig. S9C-S9F). These indicate that they are all from intrinsic magnetic origins, rather than other extrinsic effects. Besides, our field-dependent MFM studies (Fig. S10) demonstrate the robustness of MHD wall contrasts in the conical state induced by applied out-of-plane magnetic fields up to 5 tesla, which is again consistent with the Neel-type nature of MHD walls discussed above.
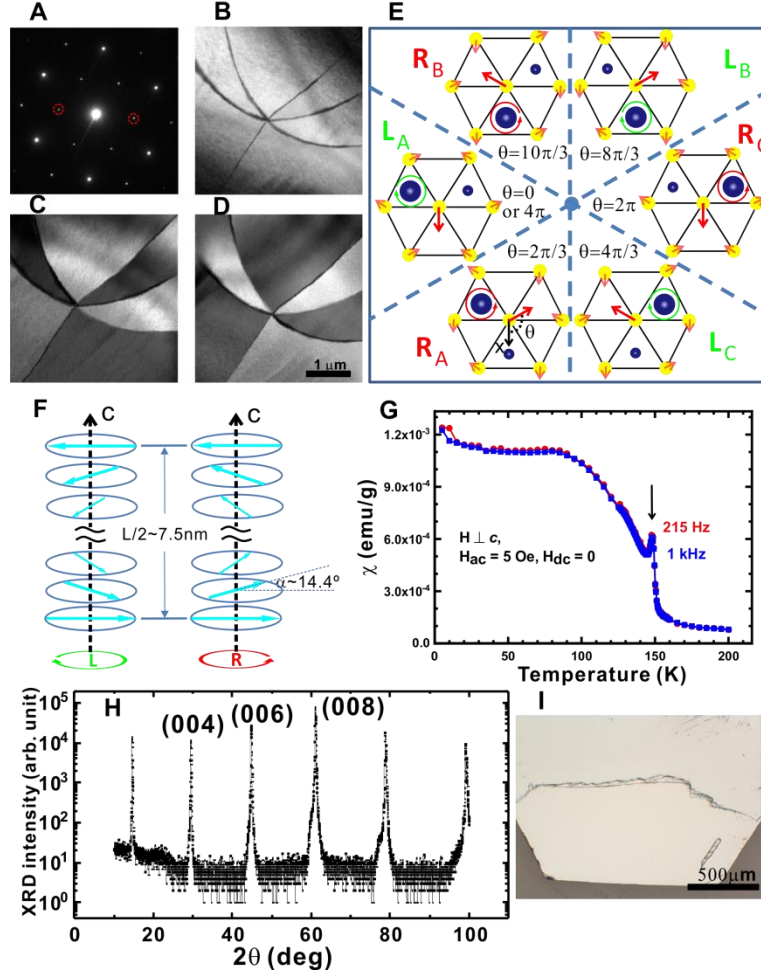
Fig. S1. Structural chirality and magnetic helicity in Cr$_{1/3}$TaS$_2$. (**A**) Selected area electron diffraction pattern revealing √3a ×√3a superlattice spots of the *P*6$_3$/mmc 2H-TaS$_2$ structure. (**B-D**) Dark-field TEM images taken using the pair of superlattice spots indicated by red dashed circles, showing a typical six structural chiral domains at different tilting conditions: (B) a weak-beam condition along [001] zone axis with a small tilting angle to enhance domain wall contrasts and (C-D) the Friedel's pair breaking conditions to demonstrate reversed domain contrasts due to a space inversion symmetry breaking. (**E**) The configuration of a structural vortex in a TaS$_2$ layer. The big (small) blue balls are Cr atoms above (beneath) the TaS$_2$ layer while other symbols are the same as those in Fig. 1A. Ta atoms are removed for simplicity. Center S atoms are supposedly identical within unit-cell translations, but their displacement directions (big red arrows) rotate $|\Delta\theta|=2\pi/3$ across each chiral domain wall. The angle θ is the misalignment of the big red arrow on the central site of the hexagon with respect to the crystallographic x axis (see bottom left sketch in E). (**F**) Schematic magnetic helical structures with different helicities. (**G**) AC magnetic susceptibility with zero DC magnetic field at different frequencies, showing a kink at the onset of the helical order. (H) X-ray diffraction of a single crystal shows clean (00L) peaks without any impurity phases. (I) Optical microscope image of an as-grown Cr$_{1/3}$TaS$_2$ crystal shows a shiny surface and the hexagonal shape.
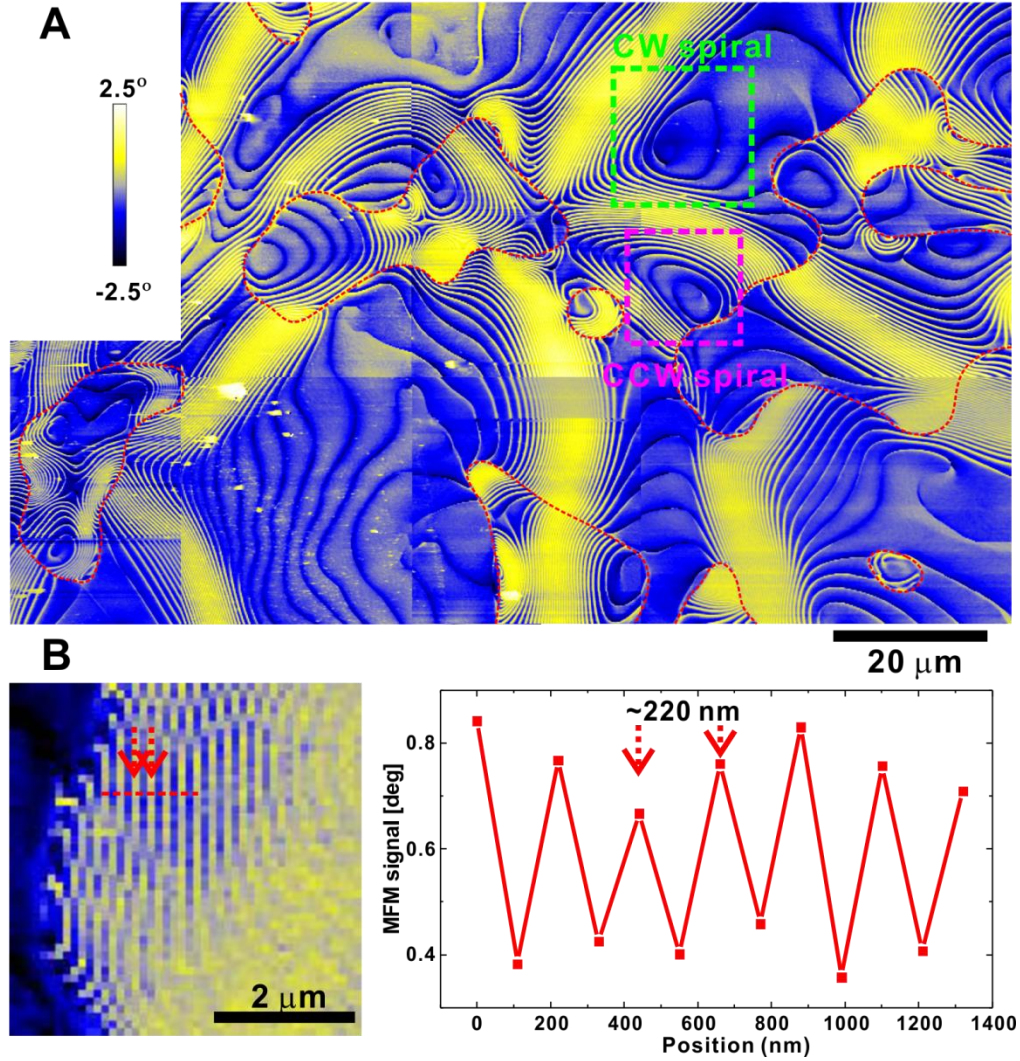
Fig. S2. Macroscopic structural chiral domains and the coexistence of spiral magnetic superstructures with different spiralities. (**A**) The merged large-scale MFM image of a slowly-cooled $Cr_{1/3}TaS_2$ specimen at 80 K, manifesting large loop-shaped structural chiral/magnetic helical domains. Structural chiral/magnetic helical domain walls are illustrated by red dashed lines. The coexistence of counter-clockwise (CCW, marked by the pink dashed square) and clockwise (CW, marked by the green dashed square) spiral magnetic superstructures is evident within large structural chiral/magnetic helical domains. The spirality of an in-plane spiral magnetic superstructure is defined by their CW or CCW path going from the center to the rim of the spiral pattern along the domain wall. (**B**) MFM image of another magnified area and its line profiles, demonstrating high-density CyMS whose spatial separation can be as small as ~220 nm or even smaller as limited by the resolution of scanning. The positions of two adjacent CyMS are marked by red dashed arrows.
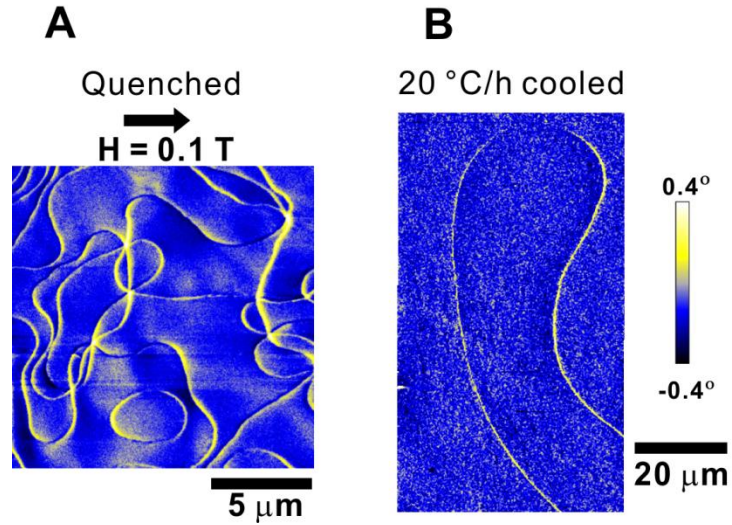
A

Quenched

H = 0.1 T

B

20 °C/h cooled

0.4°

-0.4°

5 μm

20 μm

Fig. S3. MFM domains in a large in-plane magnetic field. MFM images of **(A)** quenched and **(B)** 20°C slowly-cooled (during the chiral structural transition) $Cr_{1/3}TaS_2$ specimens at 80 K in a 1000 Oe in-plane magnetic field. The magnetic field direction is pointing from the left to the right of the image. Only structural chiral/ magnetic helical domain wall contrasts are visible in the presence of a large in-plane magnetic field. Both quenched and 20°C slowly-cooled specimens are cooled down from 300 K to 80 K in the presence of a 1000 Oe in-plane magnetic field.
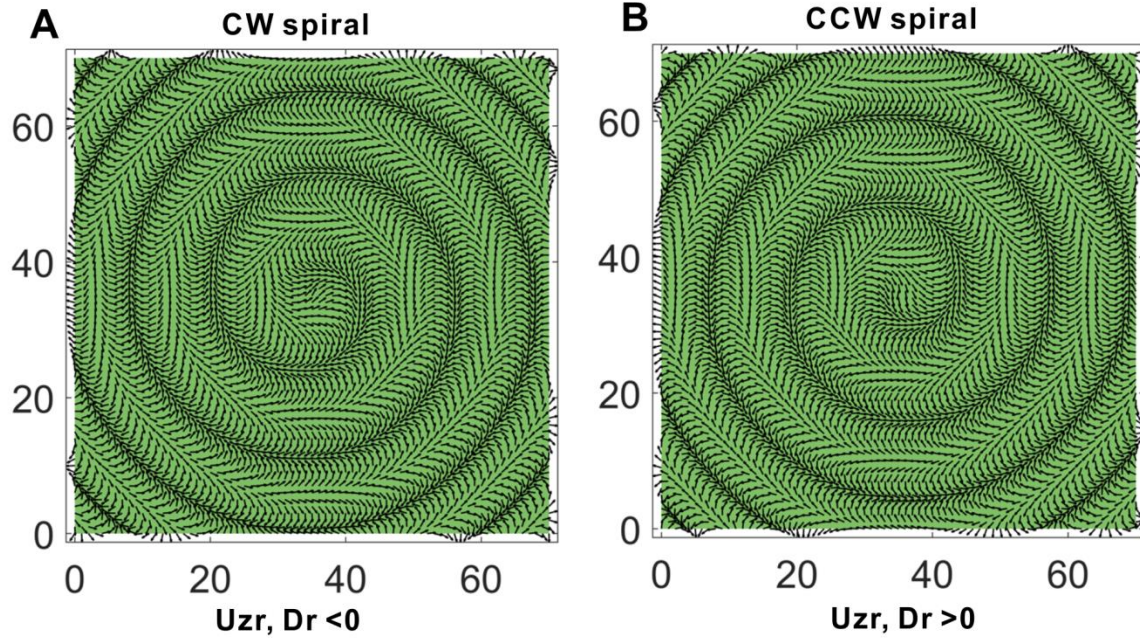
Fig. S4. The spirality and the sign of strains. Simulated final spin configurations of the top layer with a **(A)** negative and **(B)** positive sign of strain u_{zr} and induced DMI D_r, showing clockwise (CW) and counter-clockwise (CCW) spiral magnetic superstructures respectively (see Materials and Methods). The spirality of an in-plane spiral magnetic superstructure is defined by their CW or CCW path going from the center to the rim of the spiral pattern along the domain wall.
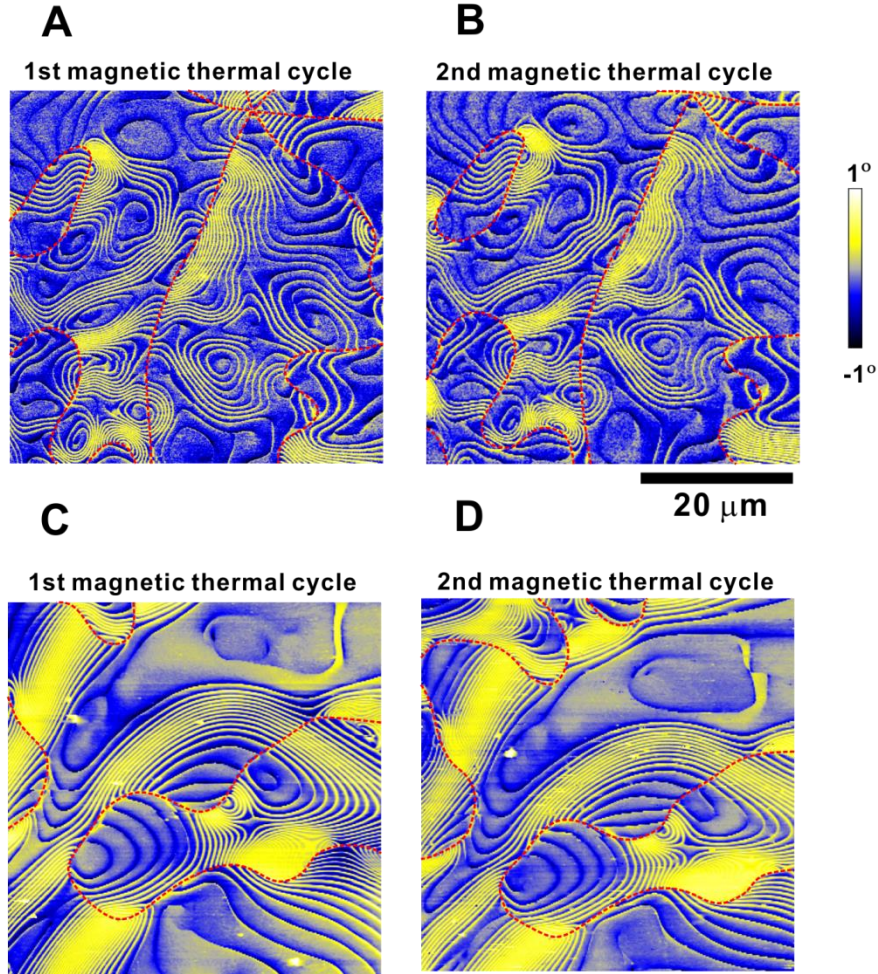
Fig. S5. Magnetic domains of slowly-cooled $Cr_{1/3}TaS_2$ in different magnetic thermal cycles. (A-B) MFM images of an area at 80 K in different magnetic thermal cycles (heating up only to 300 K). **(C-D)** MFM images of another faraway area in different magnetic thermal cycles (heating up only to 300 K). Structural chiral/magnetic helical domain walls are illustrated by red dashed lines. Similar but different domain patterns are always observed in different magnetic thermal cycles and structural chiral domain walls are intact, which implies embedded intrinsic strains are likely associated with structural chiral domain walls formed during the achiral-to-chiral transition at ~ 980°C.
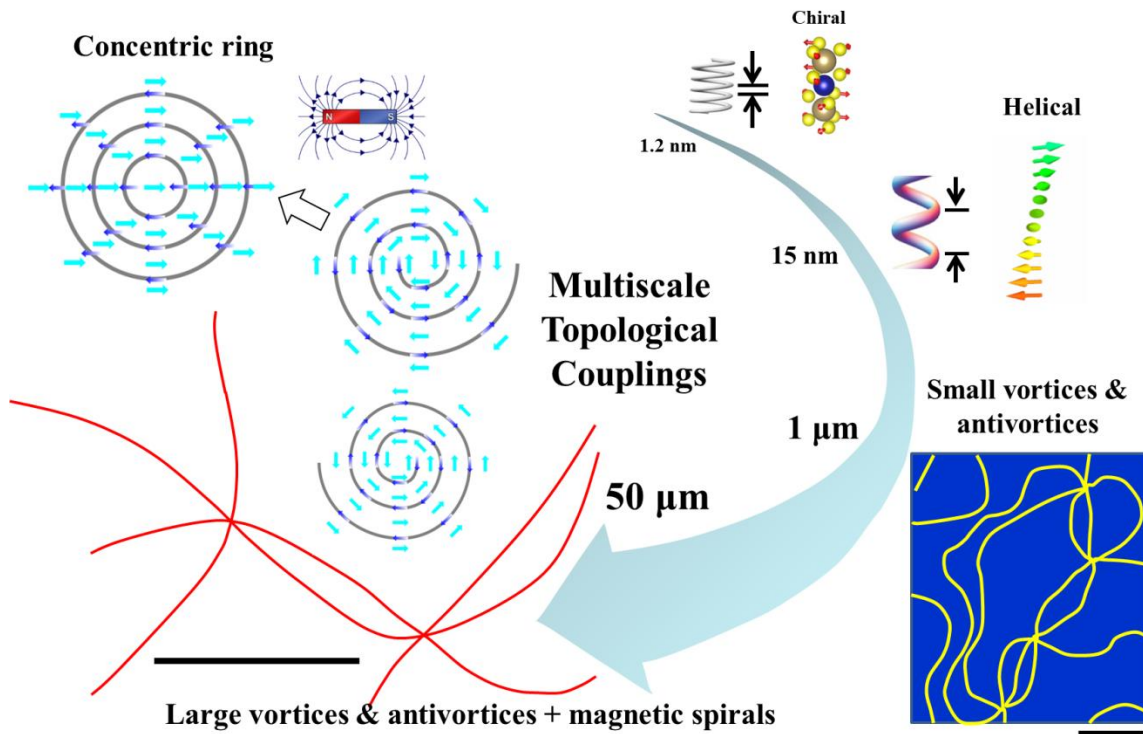
Fig. S6. Multiscale topological couplings. Schematic cartoons of topological couplings occurring at all length scales in $Cr_{1/3}TaS_2$ from the nanometer scales of structural chiral pitch (1.2 nm), magnetic helical pitch (15 nm), and CyMS pitch (~200 nm or larger) to the macroscopic scales (1-100 μm) of topological vortex domains, demonstrating rich physics of multiscale topological textures. These CyMS and spiral magnetic superstructures are found hypersensitive to external stimuli such as magnetic fields and strains. All length scales are illustrated by corresponding marked distances or scale bars.
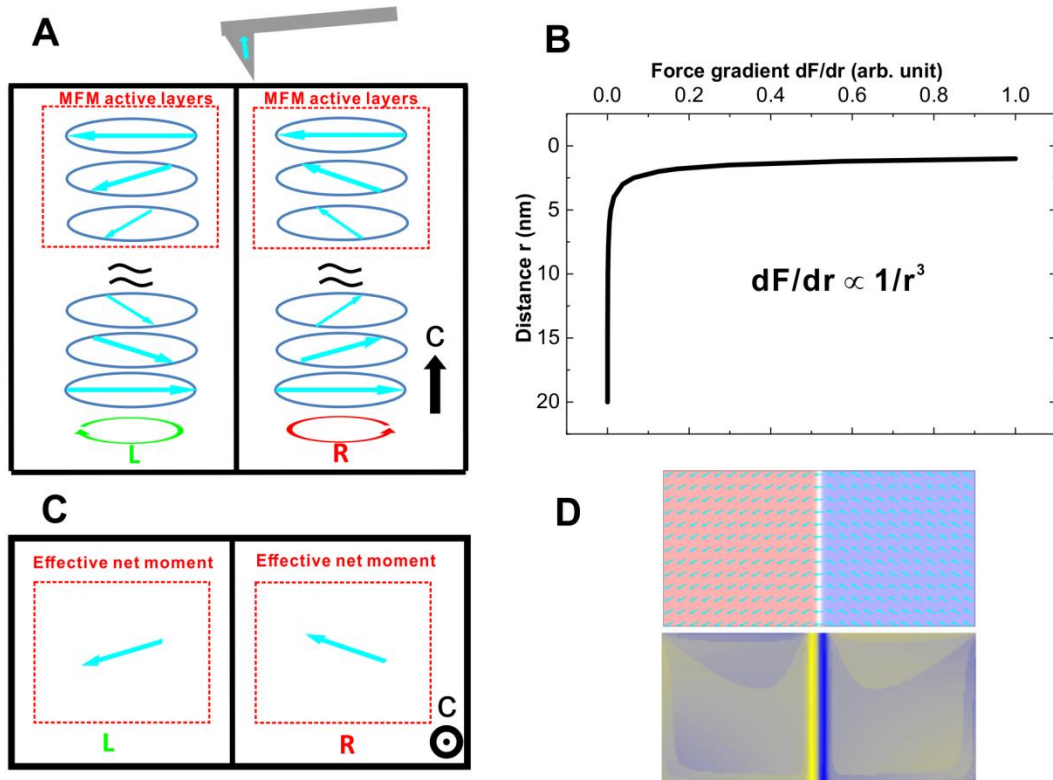
Fig. S7. MFM working mechanism on helimagnets. (**A**) Schematic image of a long helical pitch sample and its active layers for MFM measurements. (**B**) The magnetic force as a function of the measuring distance for MFM measurements. (**C**) The effective magnetic moment of long-pitch helical spins at a helical domain wall and (**D**) its corresponding simulated MFM image.
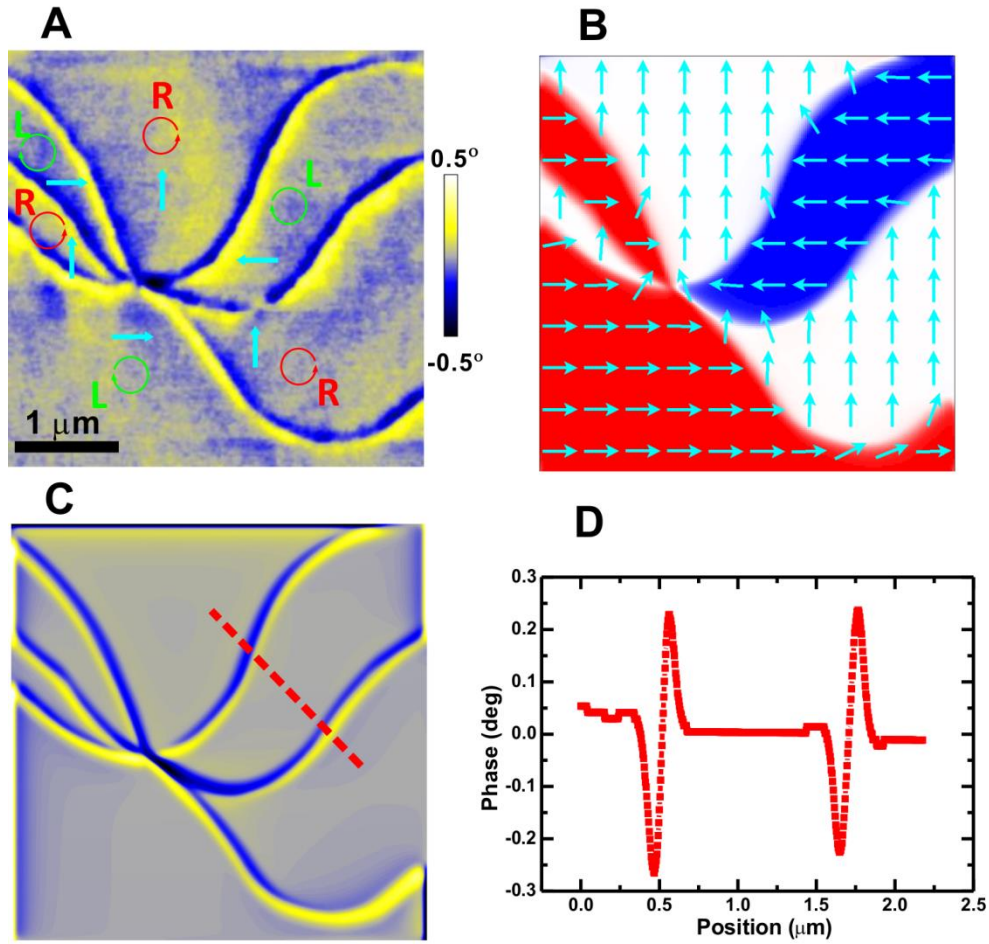
Fig. S8. Helical magnetic order and MFM simulations. (**A**) A zoomed-in MFM image of Fig. 1G and (**B**) the proposed corresponding effective magnetic moment configuration. (**C**) The simulated MFM image using the spin configuration given in (B). (**D**) The line profile of the red dashed line in (C), which is consistent with the one in Fig. 1I.
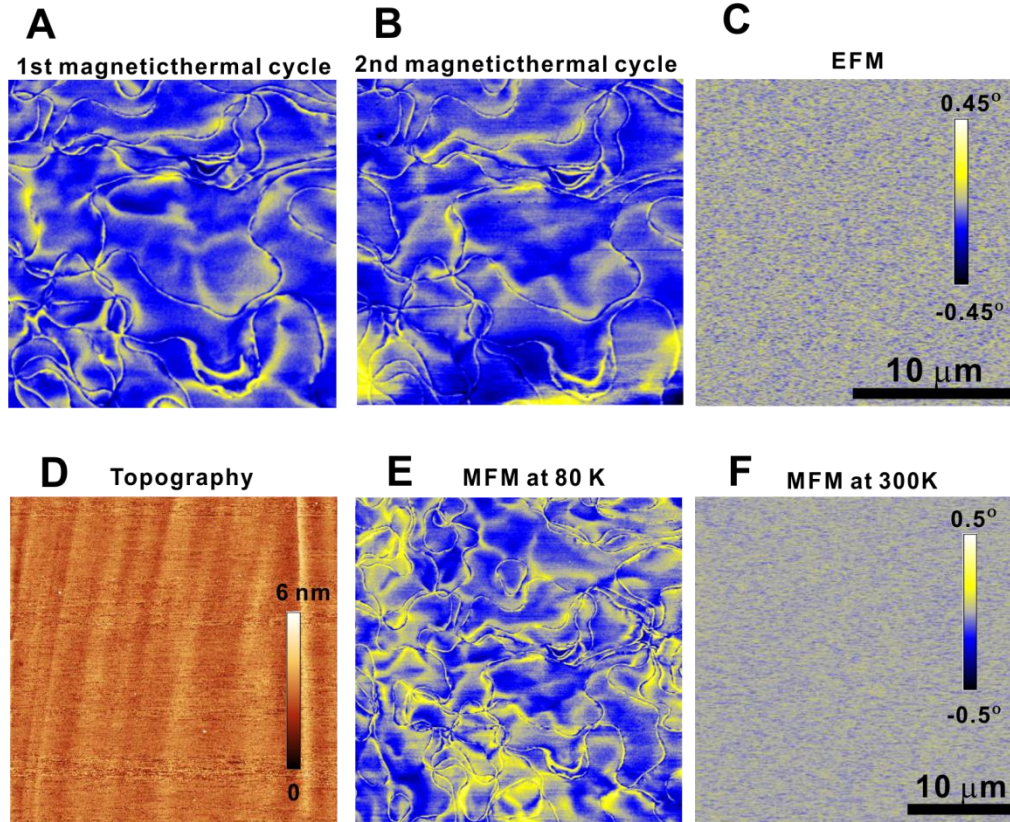
Fig. S9. Magnetic contrasts from intrinsic magnetic origins. (**A**) MFM image of a quenched $Cr_{1/3}TaS_2$ specimen at 80 K in the first magnetic thermal cycle. (**B**) MFM image of the same area at 80 K in the second magnetic thermal cycle. The specimen is heated up to 300 K between two magnetic thermal cycles. Positions of sharp magnetic helical domain walls remain intact while their contrast types and magnetic antiphase domain patterns are dissimilar in different magnetic thermal cycles, indicating magnetic helical domain walls are interlocked to structural chiral domain walls. (**C**) Electrostatic force microscopy (EFM) image of the same area scanned in (A) and (B) at 80 K using a nonmagnetic conducting tip. (**D**) The topography and the corresponding MFM images at (**E**) 80 K and (**F**) 300 K. MFM signals have no correlations with the topography and the EFM image.
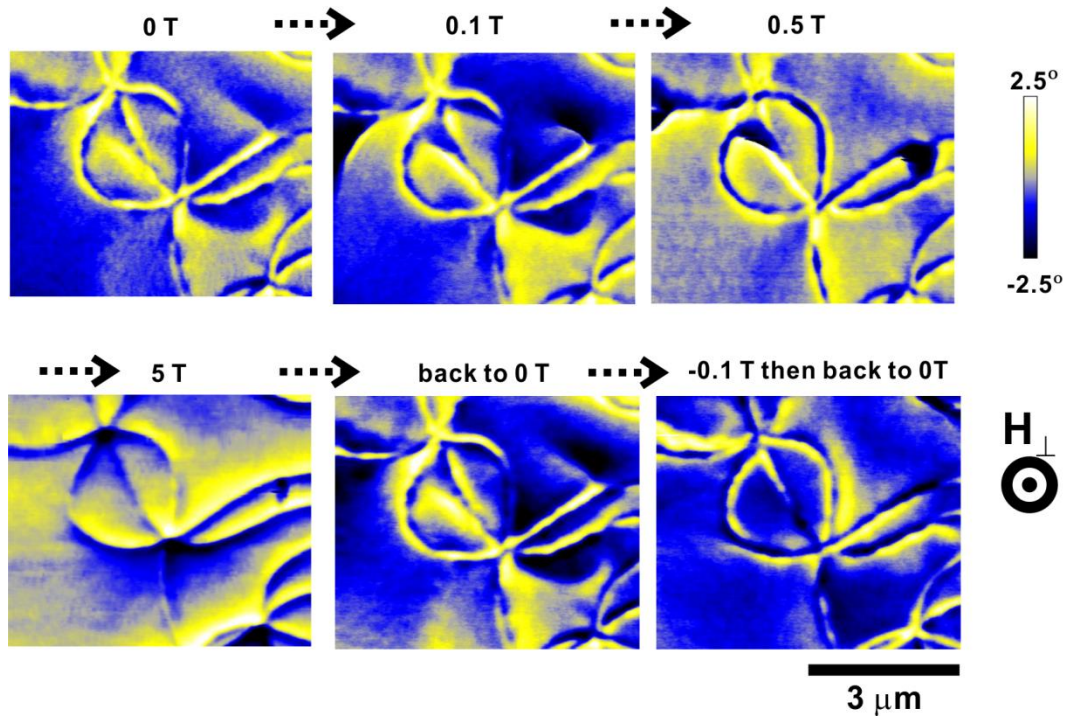
Fig. S10. Magnetic domains as a function of out-of-plane magnetic fields at 55 K. Sequential MFM images of a quenched $Cr_{1/3}TaS_2$ specimen showing clear magnetic helical domain wall contrasts up to 5 T while entering a conical state. The non-vanishing contrasts in high out-of-plane fields demonstrate the Neel-type nature of these magnetic helical domain walls.

SI References

1. J. Kim, *et al.*, Direct measurement of the magnetic penetration depth by magnetic force microscopy. *Supercond. Sci. Technol.* **25**, 112001 (2012).
2. A. Vansteenkiste, *et al.*, The design and verification of MuMax3. *AIP Adv.* **4**, 107133 (2014).
3. V. Simonet, M. Loire, R. Ballou, Magnetic chirality as probed by neutron scattering. *Eur. Phys. J. Spec. Top.* **213**, 5–36 (2012).
4. V. A. Dyadkin, *et al.*, Control of chirality of transition-metal monosilicides by the Czochralski method. *Phys. Rev. B*. **84**, 014435 (2011).